



Microstructure and Properties of AlCoCrFeNi_{2.1} Eutectic High-Entropy Alloy Coatings Fabricated by Extreme High-Speed and Conventional Laser Cladding

Jia Wang¹ · Yang Li¹ · Bingwen Lu² · Jin Liu¹ · Na Tan¹ · Yujie Zhou¹ · Yujun Cai¹ · Zichuan Lu³

Submitted: 8 September 2023 / in revised form: 6 January 2024 / Accepted: 22 January 2024 / Published online: 23 February 2024
© ASM International 2024

Abstract AlCoCrFeNi_{2.1} eutectic high-entropy alloys (HEAs) are a new kind of alloy with high entropy and eutectic properties. Their advantages in terms of strength and shape matching can be fully exploited using extreme high-speed laser cladding (EHLA). In this paper, AlCoCrFeNi_{2.1} eutectic HEA coatings were prepared by conventional laser cladding (CLA) and EHLA. The microstructures and phase compositions of the two coatings were analyzed by scanning electron microscopy, x-ray diffraction, and electron backscatter diffraction. The microhardness and wear resistance values of the coatings

were tested using a microhardness tester and a friction and wear tester, respectively. The results showed that the surface qualities of both the CLA and EHLA coatings were good and had no cracks or defects. Compared with those of the CLA coating, the EHLA coating had finer grains and a more uniform distribution. Both coatings contained face-centered cubic (FCC) and body-centered cubic (BCC) phases, but the BCC phase of the EHLA coating was less precipitated than the CLA coating. The higher microhardness and better wear resistance of the EHLA coatings occurred in the presence of Hall–Petch strengthening.

✉ Yang Li
liyang@tute.edu.cn

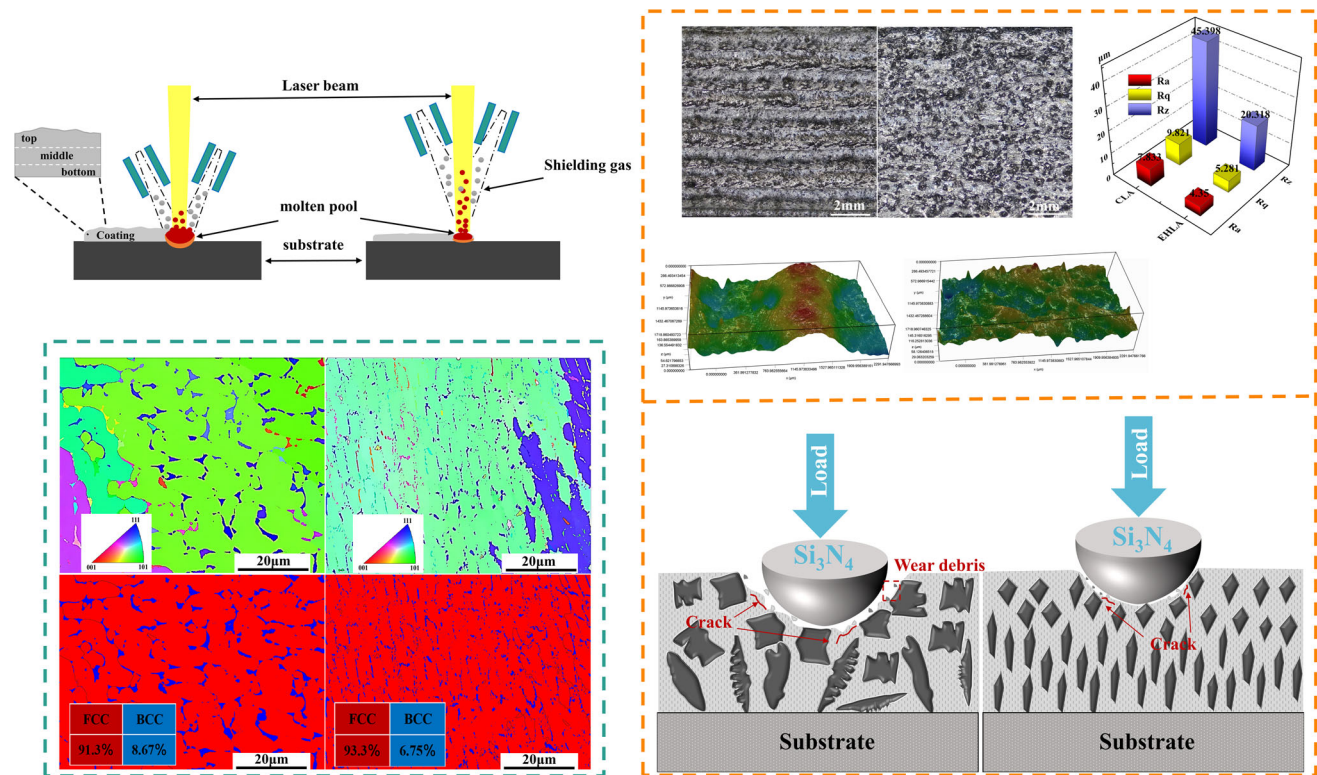
✉ Bingwen Lu
lubingwen@gdinm.com

¹ National-Local Joint Engineering Laboratory of Intelligent Manufacturing Oriented Automobile Die & Mould, Tianjin University of Technology and Education, Tianjin 300222, China

² National Engineering Laboratory of Modern Materials Surface Engineering Technology, Guangdong Provincial Key Laboratory of Modern Surface Engineering Technology, Institute of New Materials, Guangdong Academy of Sciences, Guangzhou 510651, Guangdong, China

³ Aerospace Research Institute of Materials and Processing Technology, Beijing 10076, China

Graphical Abstract



Keywords extreme high-speed laser cladding · Hall–Petch strengthening · hardness · microstructure · phase composition · wear resistance

Introduction

High-entropy alloys (HEAs) are prepared by mixing five or more elements in equal or near equal atomic ratios (Ref 1). Given the high entropy effect, hysteretic diffusion effect, lattice distortion effect, and cocktail effect on the alloy (Ref 2), HEAs show excellent mechanical properties, such as higher strength, hardness, friction, and wear resistance (Ref 3–5) than conventional alloys. In addition, the materials exhibit better tensile strength, fracture resistance, oxidation resistance, and corrosion resistance than conventional alloys and can meet the requirements of most harsh working environments and special equipment (Ref 6–9).

However, single-phase HEAs have an imbalance between their high rupture strength and ductility. Single face-centered cubic (FCC) solid-solution HEAs have high plasticity and low strength (Ref 10), and single body-centered cubic (BCC) solid-solution HEAs possess high strength and brittleness (Ref 11, 12), which hinder their

application. To further optimize the performance of alloys and solve the existing problems of HEAs, Professor Lu et al. proposed the concept of eutectic HEAs for the first time in 2014 and successfully prepared an AlCoCrFeNi_{2.1} eutectic HEA (Ref 13). The eutectic structure of the alloy is composed of an ordered FCC phase (L₁₂) and an ordered BCC phase (B₂) stacked on top of each other (Ref 14). Based on the advantages of FCC and BCC HEAs, strength and plasticity can be matched well (Ref 15, 16). However, research on eutectic high-entropy alloys is relatively limited, and most of the related research has focused on improving the mechanical properties of AlCoCrFeNi_{2.1} EHEA materials (Ref 17, 18). To date, research on this alloy is still in the exploratory stage, and research on the phase formation mechanism and microstructure evolution mechanism is insufficient.

Eutectic HEA bulk materials are generally prepared by vacuum arc melting or induction melting (Ref 19, 20). However, this preparation method has a low solidification rate and easily causes casting defects, such as shrinkage and porosity. In addition, eutectic HEAs contain precious metals, such as Co, and the direct use of bulk materials is often extremely costly. If surface engineering technology can be used to prepare eutectic HEA coatings on the surface of raw materials, the cost is greatly reduced. If

excellent surface properties can be guaranteed, a new method for industrial production can be developed. As a typical surface engineering technology, laser cladding involves the use of a wide range of optional materials, such as self-fusible alloy powder, high-entropy alloy powder, ceramic powder and composite material powder. Through the selection of different materials, coatings with excellent service performance can be obtained (Ref 21–23). The principle is to use a high-energy laser beam as a heat source to melt the alloy powder on the matrix surface and to form a metallurgically bonded coating after solidification (Ref 24, 25). Therefore, the aim of this research is to prepare AlCoCrFeNi_{2.1} HEA coatings with excellent properties on 304 stainless steel substrates by laser cladding technology.

Given that the dilution rate of conventional laser cladding (CLA) is often more than 10%, the resulting cladding layer is thick, and the surface roughness is high; thus, the cladding must be turned and ground before application, which results in material waste. In addition, in the CLA process, laser energy mainly acts on the molten pool on the substrate surface, which increases the heat input of laser energy to the substrate with a high stress (Ref 26) and leads to the generation of cracks. To solve the above problems, the Fraunhofer Institute for Laser Technology and the Research Center for Advanced Manufacturing Technology of the General Institute of Mechanical Sciences in Germany have jointly developed extreme high-speed laser cladding (EHLA) (Ref 27, 28). In contrast to CLA technology, EHLA technology uses synchronous powder delivery to control powder convergence in the laser beam above the molten pool, which allows most of the laser energy to directly act on the cladding powder. The cladding powder is in a molten or semi-molten state before it reaches the molten pool, which can shorten the duration of the powder in the molten pool (Ref 29–31). Thus, the heat input to the substrate, cladding efficiency, powder position distribution, desirable corrosion resistance, small dilution rate, and heat-affected zone are reduced (Ref 32–36). In summary, the coating prepared by EHLA technology not only achieves better metallurgical bonding with the substrate but also ensures the excellent properties of the alloy (Ref 37–40).

In this paper, with 304 stainless steel as the substrate, an AlCoCrFeNi_{2.1} eutectic HEA coating was prepared using CLA and EHLA technologies. The macroscopic morphologies, microstructures, phase distributions, and coating properties (microhardness and wear resistance) of the coatings under different preparation processes were compared to provide a basis for obtaining a high-quality cladding layer.

Experimental Materials and Methods

Material and Coating Preparation

The substrate material was 304 stainless steel (Tianjin Century Chuangyuan stainless steel Co., Ltd.) with a size of 100 × 100 × 10 mm, and the surface of the substrate was polished and cleaned before the experiments. For the substrate, p400, p800 and p1000 sandpapers (Supplier: Beijing Century Fenghua Technology Co., Specifications: Water Resistant Sandpaper p60-p2500) were used to remove rust from the steel surface layer until the surface was smooth and clean. The whole process lasted approximately 10 minutes. The substrate surface was subsequently cleaned with anhydrous ethanol and blown dry.

The cladding material was AlCoCrFeNi_{2.1} HEA powder with 99% purity (Supplier: Beijing Yanbang New Material Technology Co., Ltd.; Specification: 45–105 μm), and the composition is shown in Table 1. The coating was prepared using a YLS-4000-KC laser cladding system with a maximum power of 4 KW and a spot diameter of 2 mm (laser provider used in this test: Interpublic Group of Companies; laser type: fiber laser; laser wavelength: 1070 nm). The powder feeding method involved synchronous powder feeding, and high-purity argon was used as both the protective gas and powder feeding gas. Figure 1(a) and (b) shows the working principle. The EHLA powder was first gathered at the top of the molten pool and then melted by laser irradiation into the molten pool. The thermally affected area generated by the EHLA powder was considerably smaller than that produced by the CLA. Thus, the effect on the substrate was reduced, and the cladding efficiency was improved. Table 2 shows the process parameters of the two coatings.

Test Methods

After the preparation of the coating, to facilitate the following observation and testing, we first cut the bulk coating into 10 × 10 × 10 mm samples using a wire cutting machine and then ground and polished them. The detailed steps were as follows. First, the cross sections of the specimens were ground with p240–p2000 sandpaper to ensure that the scratch direction was consistent, and each specimen was ground for at least 30 minutes. Second, the coatings were polished with a diamond polishing agent

Table 1 Composition of the AlCoCrFeNi_{2.1} HEA, at.%

Ele.	Al	Co	Cr	Fe	Ni
at.%	16.39	16.39	16.39	16.40	34.43

Fig. 1 Working principles of the CLA and EHLA coatings: (a) CLA and (b) EHLA.

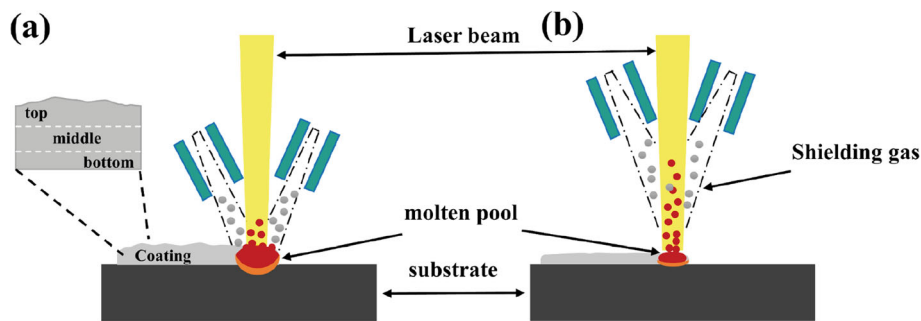


Table 2 CLA and EHLA process parameters

Process parameter	CLA	EHLA
Laser powder, W	1200	2500
Laser scanning speed, mm/s	20	400
Overlapping, %	50	85
Powder delivery rate, g/min	17	17
Shielding gas flow, L/min	15	15
Powder delivery flow, L/min	10	10
Spot diameter, mm	2	2
Passes	40	10

(2.5 μm), and the polishing cloth was used until the scratches disappeared (polishing cloth, supplier: MEGA Instruments (Suzhou) Co., Ltd.; specifications: red synthetic fiber polishing cloth (1.0–3.5 μm); diamond spray polishing (2.5 μm): Zhejiang Yiwu Lixie Instrument Equipment Co.; silica polishing suspension (0.06 μm): Buehler). Finally, the coating was etched with aqua regia (etching time: 10–12 s). As shown in Fig. 1, the microstructures of the different regions (top, middle, and bottom) of the two samples were observed by scanning electron microscopy (SEM; Zeiss Sigma300). The phase compositions of the two coatings were characterized by an X’Pert PRO x-ray diffractometer. Field-emission SEM (Zeiss, Gemini-300) equipment was used for electron backscatter diffraction (EBSD) to characterize the grain orientation and phase distribution of the coating. The samples were first cut into flat shapes of suitable sizes, subsequently mounted with conductive resin, polished with a diamond polishing agent, and polished with a silica polishing suspension to meet the requirements of the EBSD test sample. An HVS-1000 Vickers hardness tester was used to measure the hardnesses of the two coatings. The load was 500 g, the loading time was 10 s, and the test area was from the top of the coating to the substrate.

The dry sliding friction and wear tests were carried out in a friction and wear testing machine (BRUKER UMT-5)

at room temperature. A grinding ball made of Si₃N₄ (6 mm diameter) was selected. The test time was 60 min under a 15-N load, and the frequency was 1 Hz. After the experiment, a BRUKER Contour GT-K and Zeiss Sigma300 scanning electron microscope were used to detect and analyze the morphologies of the wear tracks, respectively. The average friction coefficient and average wear volume were measured to compare the wear resistance of the two coatings.

Results and Discussion

Macromorphological Analysis

As shown in Fig. 2, the coatings exhibited desirable surface quality and no cracks. The surface roughness of the coating prepared by EHLA was more compact and uniform than that of the coating prepared using CLA. This difference was observed because the EHLA technology adjusted the convergence position of the laser, powder, and molten pool, which resulted in greater convergence of the powder than that of the upper surface of the molten pool. The converged powder was melted by laser irradiation and entered the molten pool. The surface of the prepared coating had less sticky powder and was flatter than that of CLA. Moreover, a high overlap rate could reduce the surface roughness of the coating.

Microstructural and Elemental Distributions

Energy-dispersive spectroscopy (EDS) line scanning was used to determine the transition regions and nearby elemental distributions of the two coatings. According to the EDS line scanning test results for the two coatings (Fig. 3b and d), the transition regions of the CLA and EHLA coatings were approximately 55 and 16 μm in length, respectively. Combined with the elemental Fe content shown in Table 3 and Fig. 3(e), these findings indicated that the heat input of the substrate material was low during the EHLA process, which further reduced the influence of

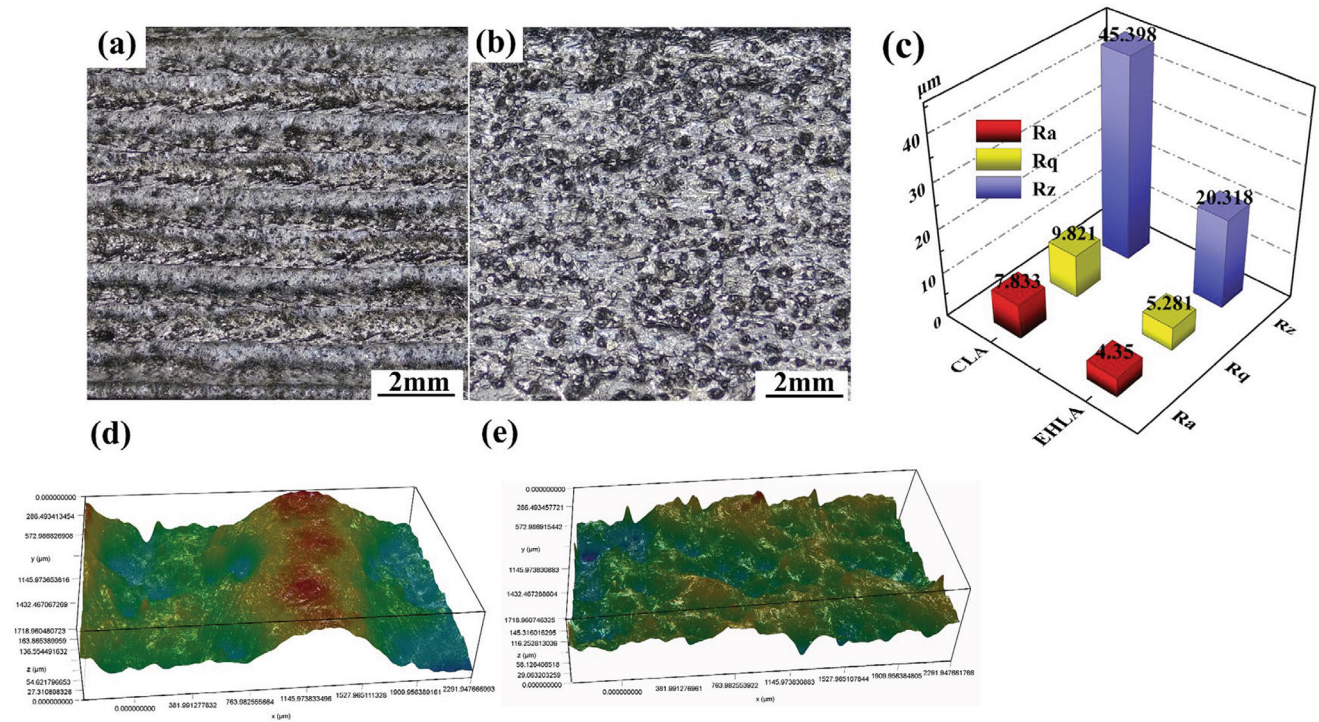


Fig. 2 Macromorphologies of the coatings: (a) (d) CLA coating and (b) (e) EHLA coating. (c) Surface roughness.

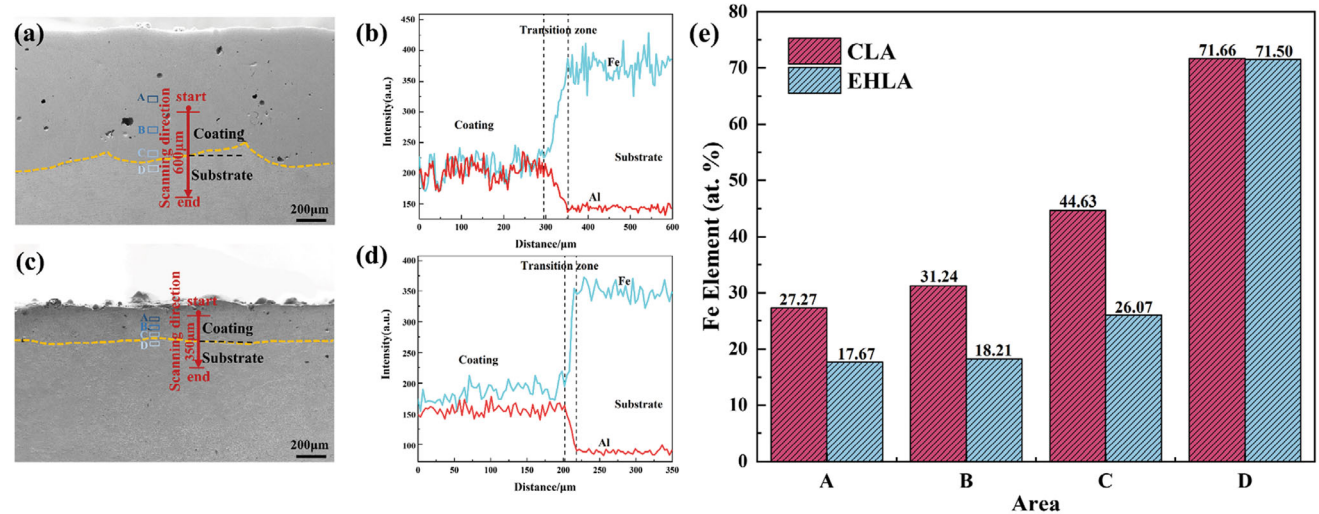


Fig. 3 EDS line scan test positions and CLA and EHLA coating test results. (a) SEM images of the CLA coatings, (b) CLA coating scan results, (c) SEM images of the EHLA coating, (d) EHLA coating scan results, and (e) Fe content at different locations on the coating.

Fe on the coating; thus, the dilution rates (CLA: 66%, EHLA: 39%) of the coatings decreased (Ref 29).

The cross-sectional morphologies of the coatings were observed via SEM. The coatings prepared by CLA and EHLA were free of cracks after the optimization of the preparation parameters, as shown in Fig. 5. The coating prepared by EHLA was notably thinner (average thickness of 226 μm , standard deviation of 14 μm , as shown in Fig. 4) than the coating prepared by CLA (average thickness of 862 μm , standard deviation of 28 μm). Moreover,

the porosity of the EHLA coating was lower (EHLA: 0.2%, CLA: 1%). This finding could be explained as follows. During the laser cladding process, the volatilization of low melting point metals or defects inside the powder itself (hollow powder) could generate gas in the melt pool. In addition, due to the large and deep melt pool of the CLA, the cooling rate was slower than that of the EHLA. Therefore, some of the gases could not be discharged quickly during the cooling process, thus increasing the porosity after solidification.

Table 3 Elemental distributions at different positions in the CLA and EHLA coatings, at.%

Area	Process method	Fe	Co	Cr	Al	Ni
A	CLA	27.27	13.32	17.54	13.27	28.61
	EHLA	17.67	16.09	16.74	16.63	32.87
B	CLA	31.24	12.22	17.61	12.19	26.74
	EHLA	18.21	15.77	16.81	16.33	32.88
C	CLA	44.63	8.53	18.65	7.94	20.25
	EHLA	26.07	13.66	17.38	13.80	29.09
D	CLA	71.66	0.53	20.30	0.00	7.51
	EHLA	71.50	0.51	20.36	0.00	7.63

Fig. 4 CLA and EHLA coating thicknesses.

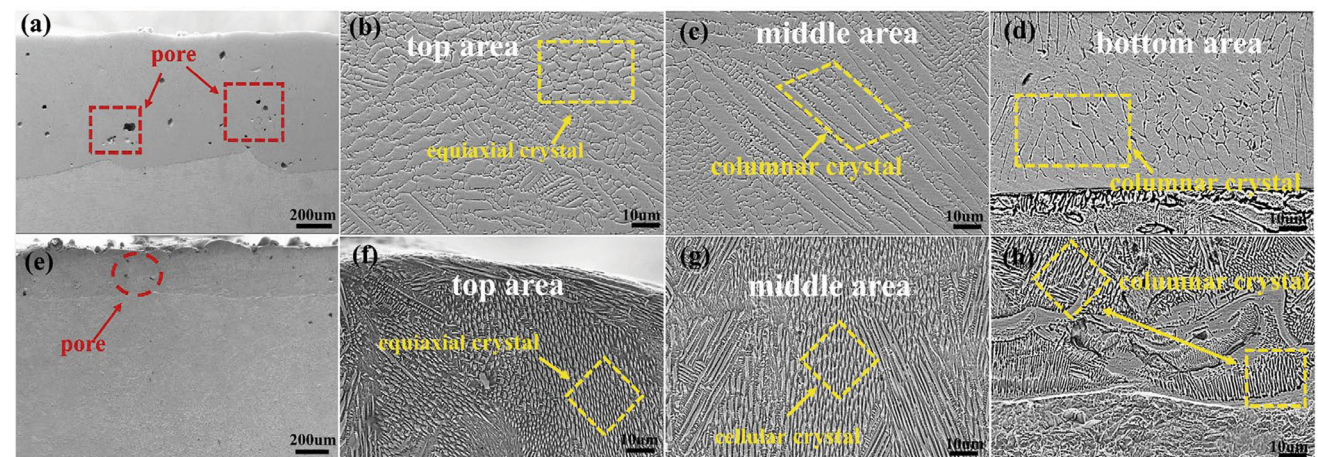
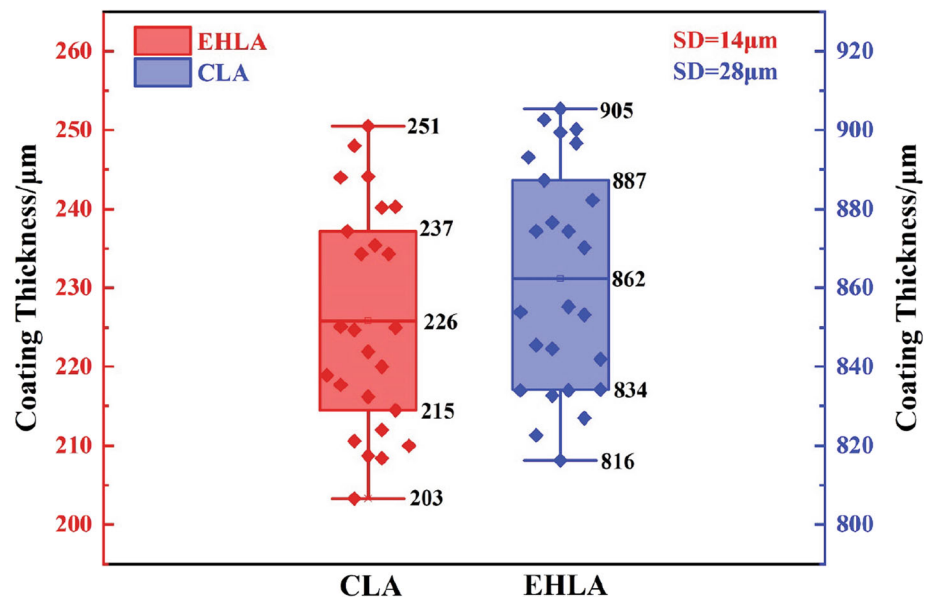
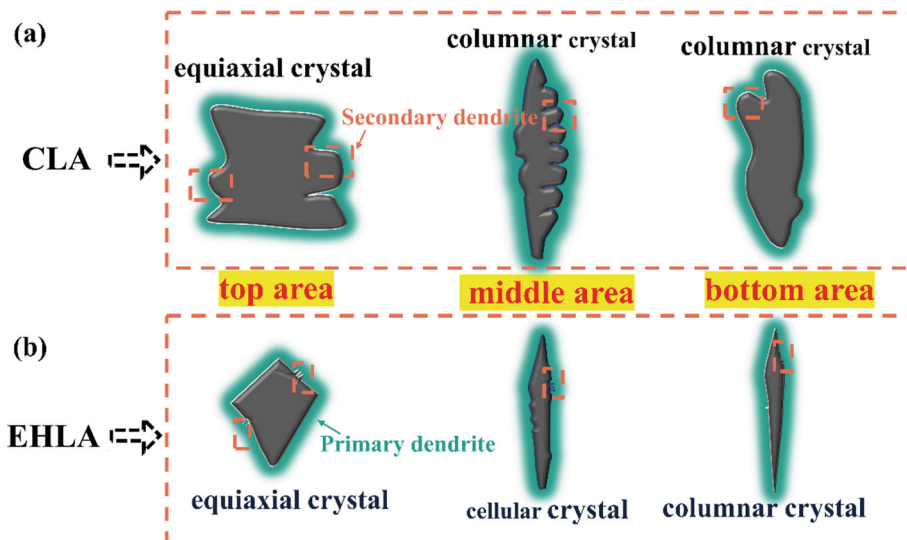


Fig. 5 Comparison of the CLA and EHLA coatings. (a) cross-sectional morphology of the CLA coating, (b) top structure of the CLA coating, (c) middle structure of the CLA coating, (d) bottom

A comparison of the microstructures of the two cladding coatings (Fig. 5) revealed that the changes in dendrite composition were the same, and the changes ranged from cellular or columnar crystals to equiaxial crystals along the heat dissipation direction. This difference arose due to the large differences between the temperature gradient and cooling rate in the depth direction of the molten pool during laser cladding (Ref 32). The cladding structure clearly resulted in stratification. Figure 5(d) and (h) shows that the bottom regions of the two cladding coatings were dominated by columnar crystals due to the large difference between the temperature gradient and cooling rate in the depth direction of the molten pool during laser cladding. When the molten

area of the CLA coating, (e) EHLA coating cross-sectional morphology, (f) top structure of the EHLA coating, (g) central structure of the EHLA coating, and (h) bottom area of the EHLA coating.

Fig. 6 Schematic of CLA and EHLA dendrites: (a) CLA dendrites and (b) EHLA dendrites.



pool solidified, as a result of contact with the cold metal in the matrix, a large temperature gradient was observed. The instantaneous crystallization rate at the interface was low, and the G/R ratio increased (G : temperature gradient, R : grain growth rate; the ratio between the temperature gradient and grain growth rate (G/R) determines the morphologies of solidified grains), which promoted the formation of columnar crystals. As the crystallization process progressed, the solid–liquid mixture gradually advanced to the middle of the molten pool (Fig. 5c and g). At this point, the microstructure of the EHLA coating was dominated by cellular crystals. This finding could be explained as follows. As the solidification rate gradually increased, the temperature gradient decreased, which initiated the phenomenon of component supercooling that led to the formation of cellular crystals. Figure 5(b) and (f) reveals that equiaxial crystals appeared in both cladding coatings because the temperature gradient decreased further as the crystallization process progressed again. In addition, as the solidification rate further increased, a more evident subcooling phenomenon occurred, which promoted the formation of equiaxial crystals (Ref 33, 34).

As determined from the schematic diagram of the CLA and EHLA dendrite changes in Fig. 6, primary and secondary dendrites appeared in the microstructures of both coatings, but the arms of the primary and secondary dendrites in the CLA were thicker and farther apart. The distance between secondary dendrite arms (λ_2) was calculated as follows:

$$\lambda_2 = A(G \times R)^{-n}$$

where A and n are material constants and $G \times R$ is the cooling rate. For the same material, A and n are fixed values; thus, the distance between secondary dendrite arms is inversely proportional to the temperature gradient, growth rate, and cooling rate. Given that EHLA had a

higher cooling rate than CLA, the coarsening time of the secondary dendrite arms was shorter, and the secondary dendrite spacing was smaller. According to solidification theory (Ref 30), the faster the cooling rate was, the greater the heat dissipation capacity at the solid–liquid interface. The insufficient growth of crystal nuclei during solidification often resulted in fine dendrite arrangements. Therefore, the dendrites of the EHLA coating were smaller and more evenly distributed than those of the CLA coating.

Phase Composition

As shown by the x-ray diffraction (XRD) patterns of the CLA and EHLA coatings in Fig. 7, the BCC diffraction peaks of both coatings were weaker than those of the powders themselves, possibly because of the following reasons. (1) During the laser cladding process, the solid solubility of the eutectic AlCoCrFeNi_{2.1} powder alloy was improved by rapid solidification (Al had a stabilizing effect on the BCC phase), and more Al entered the FCC phase in the form of a solid solution, leading to the rapid reduction or disappearance of the BCC phase. (2) The rapid heating and solidification of the AlCoCrFeNi_{2.1} powders not only caused supersaturation but also increased lattice distortion. The presence of lattice distortion further enhanced diffuse scattering, and supersaturation inhibited the precipitation of the BCC phase.

EHLA resulted in less BCC phase precipitation than CLA because the EHLA pool was small and shallow, and the melting to solidification time of the coating was short, which resulted in a fast cooling rate leading to the diffusion of eutectic alloying elements. Thus, only a small amount of BCC formed during the coprecipitation of FCC. In contrast, in the CLA, the duration of the molten pool was longer, and the solidification rate of the molten metal was

Fig. 7 XRD patterns of the coatings and powders.

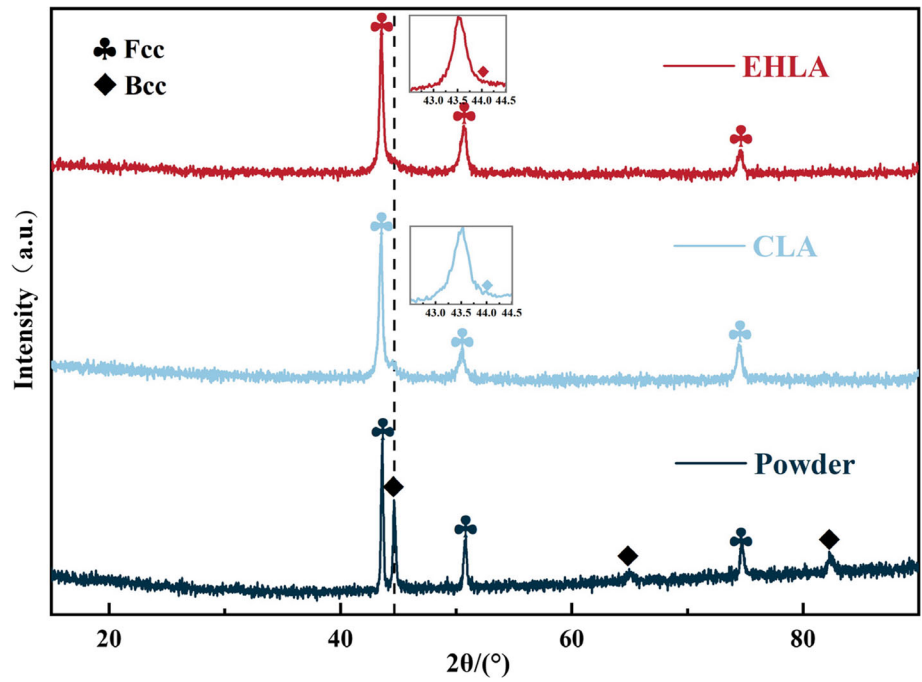
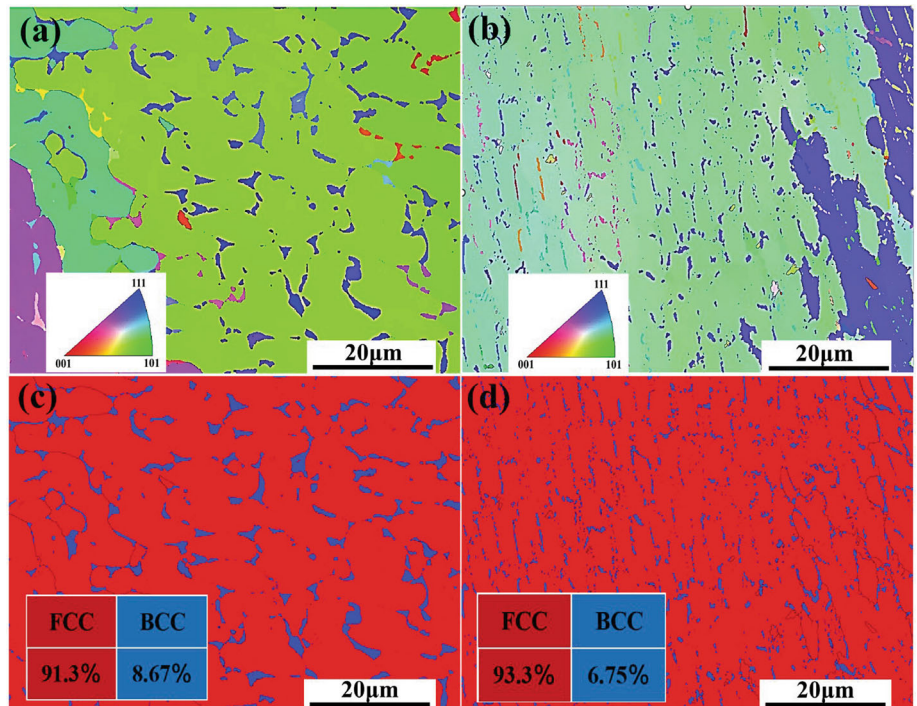


Fig. 8 EBSD characterization of the $\text{AlCoCrFeNi}_{2.1}$ coating: (a) IPF diagram of the CLA coating, (b) phase distribution of the CLA coating, (c) IPF diagram of the EHLA coating, and (d) phase distribution of the EHLA coating.



lower than that in the EHLA. Thus, more of the BCC phase precipitated.

To better compare the differences between the CLA and EHLA coatings, we characterized the grain orientations and phase distributions of the $\text{AlCoCrFeNi}_{2.1}$ coatings using EBSD. Figure 8(a) and (b) presents the inverse pole figures of the CLA and EHLA coatings, respectively. The

different colors represent the various grain orientations. The grain orientations of the two coatings were overall consistent rather than randomly distributed, and the average grain size of the EHLA coating was smaller. This result mainly occurred due to the higher cooling rate of EHLA, which promoted grain refinement. Figure 8(c) and (d) shows the detection results for the traditional and

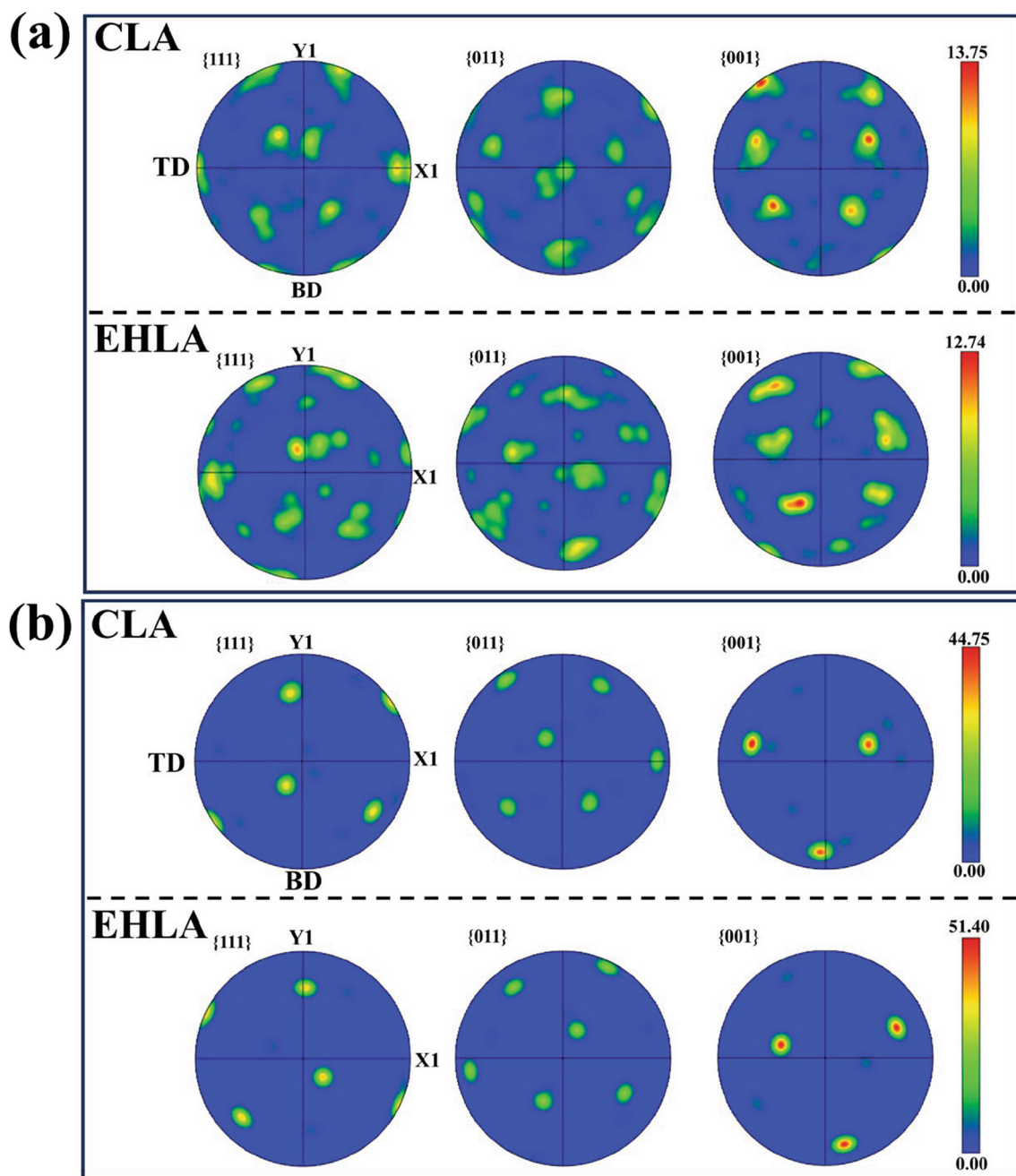


Fig. 9 Pole figures of the CLA and EHLA coatings: (a) FCC phase diagram of the CLA and EHLA coatings and (b) CLA and EHLA coating BCC phase pole diagram. BD: build direction, TD: transverse direction.

EHLA coating phases, respectively, with red and blue colors representing the FCC and BCC phases, respectively. As shown in the figures, both coatings were composed of simple solid solutions, including FCC and BCC phases. The FCC phase occupied most of the area, the BCC phase was mainly distributed between adjacent FCC grains, and the FCC phase of the EHLA coating accounted for a greater proportion of the total FCC phase, which was consistent with the XRD pattern. Thus, an increase in the

cladding speed could inhibit the generation of the BCC phase to a certain extent.

Figure 9 shows the pole figures of the FCC and BCC phases of the CLA and EHLA coatings. Both figures showed a strong preference for the $\{001\}$ texture. In the FCC phase, the $\{001\}$ texture was aligned with the build direction (BD) and transverse direction (TD). In addition, the texture indices of the BD and TD were 44.75 and 51.40, respectively. In the BCC phase, the $\{001\}$

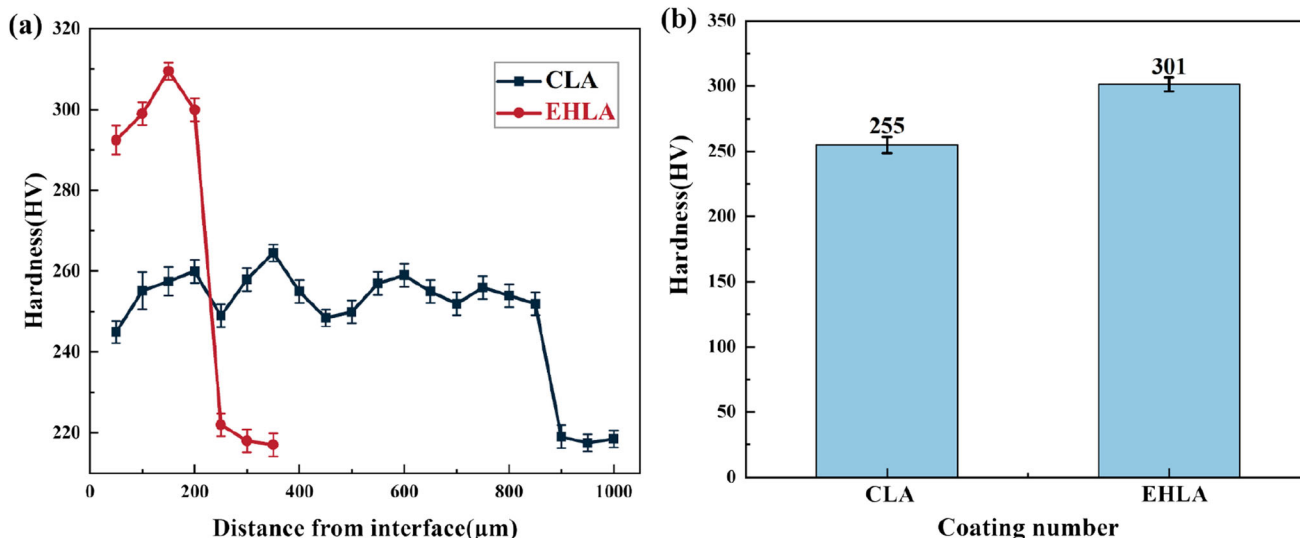


Fig. 10 Hardness distributions of the CLA and EHLA coatings: (a) microhardness curve of the coating and (b) average microhardness value of the coating.

texture was more aligned with the BD than the TD. Moreover, the texture indices were 13.75 and 12.74 for the BD and TD, respectively. The texture index represents the texture strength of the crystal to a certain extent. The different texture indices of the two coatings in the FCC and BCC phases could be related to the distributions of the two phases in the coating.

Microhardness

According to Fig. 10, based on the hardness distributions of the CLA and EHLA coatings, the hardness values of the EHLA coatings were greater than those of the CLA coatings (CLA: average hardness of 255 HV, standard deviation of 10 HV; EHLA: average hardness of 301 HV, standard deviation of 9 HV). First, these findings could be attributed to the faster cooling rate of the EHLA coating, resulting in a lower porosity and crack formation rate. This trend could increase the hardness of the coatings to a certain extent. In addition, this increase arose due to the suppression of secondary dendritic coarsening. Moreover, the spacing of the dendrite arms decreased, which resulted in a fine dendrite arrangement and subsequently increased the hardness of the coating through fine-grain strengthening (Ref 21, 22). In addition, the CLA coating had a high dilution rate (CLA: 66%, EHLA: 39%), and additional Fe diffused from the matrix into the coating, which resulted in the hardness being lower than that of the EHLA coating.

Wear Resistance

As shown in Fig. 11(a), the changes in the friction coefficients of the CLA and EHLA coatings revealed that both

coatings experienced running-in and stable wear stages. In the running-in stage, the friction mode was point contact because of the large contact stress. In addition, the friction coefficients of the two coatings increased rapidly to approximately 0.7. In the stable wear stage, given that the contact mode changed to surface contact, the contact stress decreased; thus, the friction coefficient remained relatively stable and exhibited fewer periodic fluctuations. Figure 11(b) shows that the average friction coefficients of the two coatings were almost the same: 0.6996 (CLA) and 0.7001 (EHLA). This finding could be attributed to the wear mechanisms of the two coatings, which changed simultaneously during friction and wear. In addition, the preferred grain orientation had a small influence. Therefore, the friction coefficients were roughly the same.

As shown in Fig. 12(a), (b), and (c), compared with those of the EHLA coating, the wear marks of the EHLA coating were narrower and shallower, and the wear amount was lower. The wear rates of both coatings were further calculated. The wear rate of the CLA coating was $6.19 \times 10^2 \text{ mm}^3/(\text{N m})$, while the wear rate of the EHLA coating was $5.24 \times 10^2 \text{ mm}^3/(\text{N m})$. The results showed that the wear rate of the EHLA coating was reduced by 15%. The reason for this phenomenon was that the higher hardness of the EHLA coating (according to Archard’s theory, the wear resistance of a material usually increased with increasing hardness) led to a reduction in the wear rate and an increase in the wear resistance. Figure 13 shows the surface morphologies of the wear marks on the coating. Figure 13(a) and (b) reveals that deep furrows, cracks, and coating peeling occurred on the wear marks of the CLA coating, which indicated that the wear was abrasive and adhesive (Ref 26, 27). These results were mainly due to the

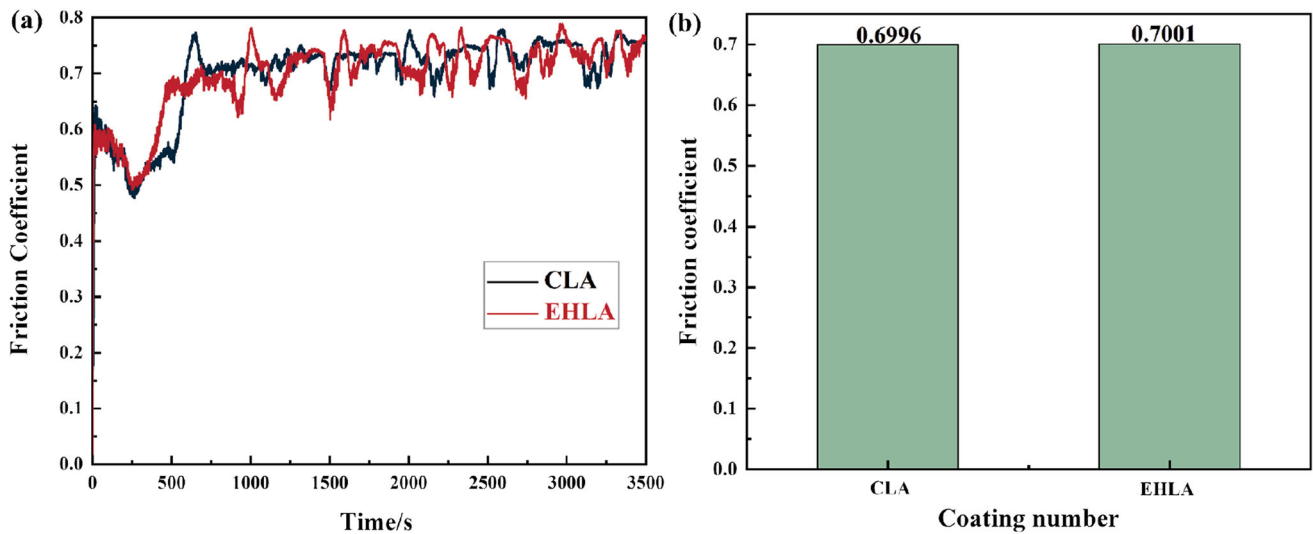


Fig. 11 Changes in the friction coefficient of the CLA and EHLA coatings: (a) changes in the friction coefficient with time and (b) average coefficient of friction.

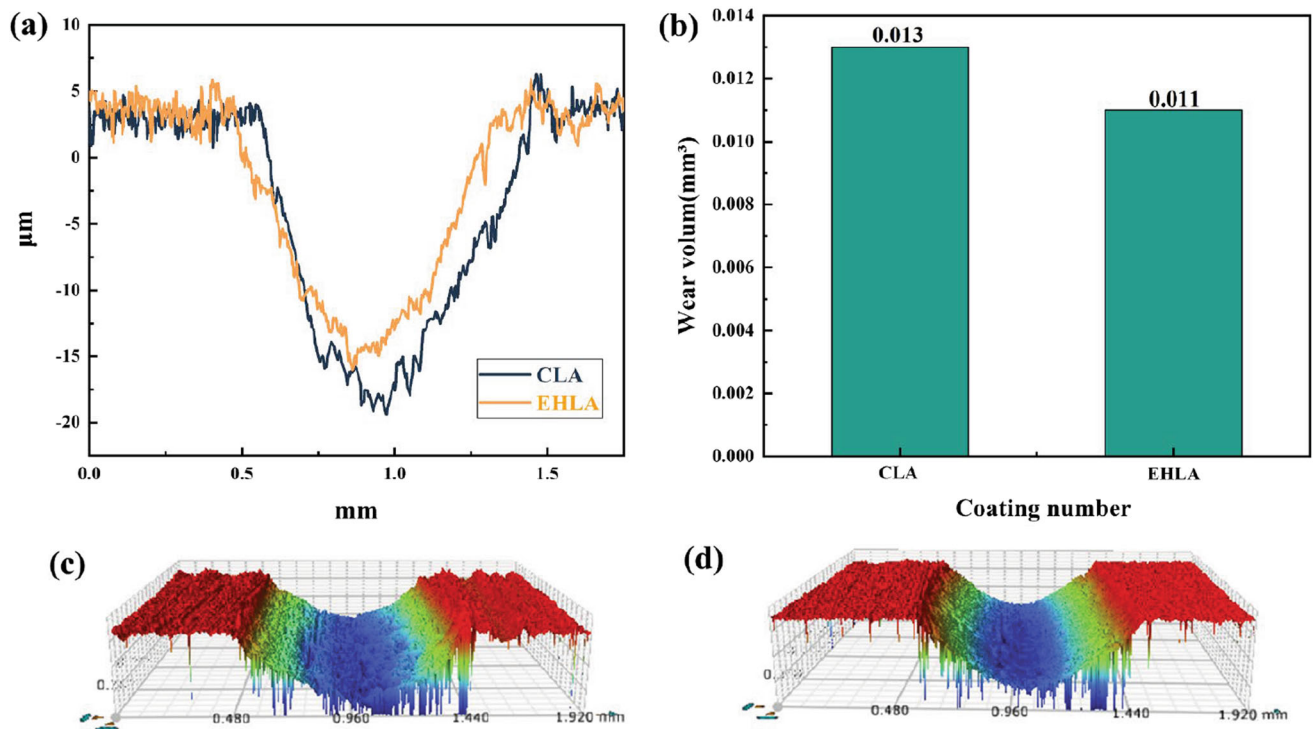


Fig. 12 Morphologies and wear amounts of the CLA and EHLA coatings: (a) abrasion depth; (b) wear volume; (c) CLA coating; and (d) EHLA coating.

slow cooling rate of the CLA coating, evident coarsening of the primary dendrites and secondary dendrite arms within the coating, and the long distance between them, which resulted in a coarse and disorderly dendrite arrangement. Moreover, the relatively coarse structures fell off during the wear process due to their low strengths, formed furrows, cracks, and plastic deformation on the

surface of the coating. As shown in Fig. 13(c) and (d), the furrow of the EHLA coating was shallow, and a few cracks and shedding were observed, which indicated that the wear modes of the EHLA coating were mainly abrasive wear and mild adhesive wear. Further SEM analysis was conducted on the worn surface, and Table 4 shows that oxidative wear occurred on both coatings. However, the

Fig. 13 Wear surface morphologies of the CLA and EHLA coatings: (a) and (b) CLA coatings and (c) and (d) EHLA coating.

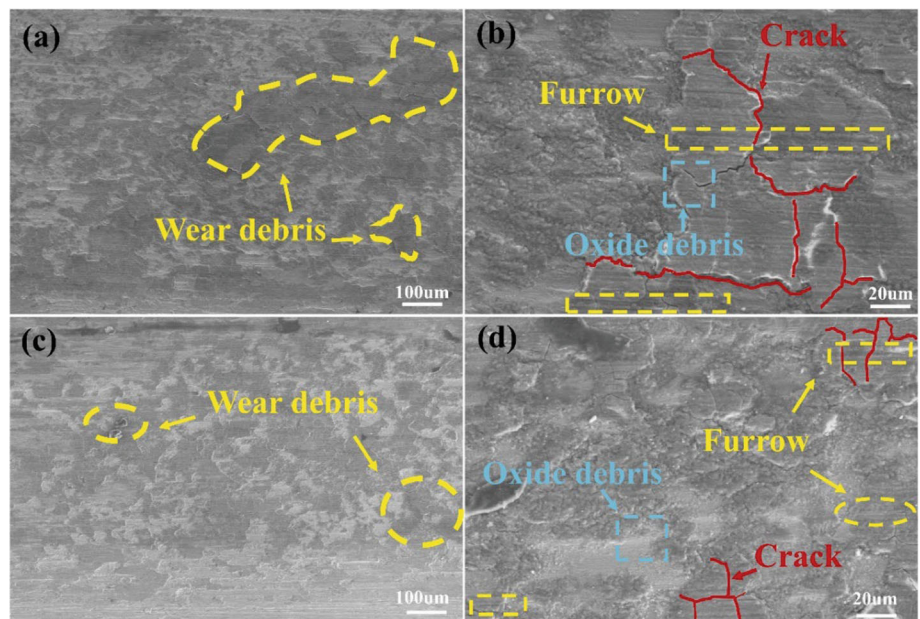


Table 4 Contents of each element in the oxide chips in Fig. 12(b) and (d)

Ele.	O	Al	Co	Cr	Fe	Ni
CLA	57.91	5.47	5.65	7.15	11.38	12.45
EHLA	41.15	8.55	9.44	10.27	10.98	19.61

oxidation degree of the EHLA coating was lower; thus, its oxidative wear was alleviated.

Figure 14 shows the wear mechanism of the two coatings. During the initial stage of wear, metal oxide wear fragments were constantly generated on the surface of the AlCoCrFeNi_{2.1}EHEA coating. Most of these wear fragments were discharged in the direction of reciprocating friction, while some of the nondischarged wear fragments accumulated on the coating surface to form a friction layer. The regathering of abrasive debris and adhesion to the coating surface had a certain protective effect on the coating to improve the wear resistance. With the extension of wear time and increase in the number of friction cycles, the oxide layer was gradually destroyed. In addition, deep furrows, cracks and coating peeling appeared on the surface of the coating. Therefore, adhesive wear, abrasive wear and oxidation wear occurred in both coatings. Although the wear mechanisms of the two coatings were the same, the EHLA coating showed better wear resistance at all stages of the wear process when combined with the morphology and oxygen content of the wear surface.

In summary, EHLA technology could improve the wear resistance of coatings to a certain extent, mainly due to the high cooling rate. This phenomenon led to the coating

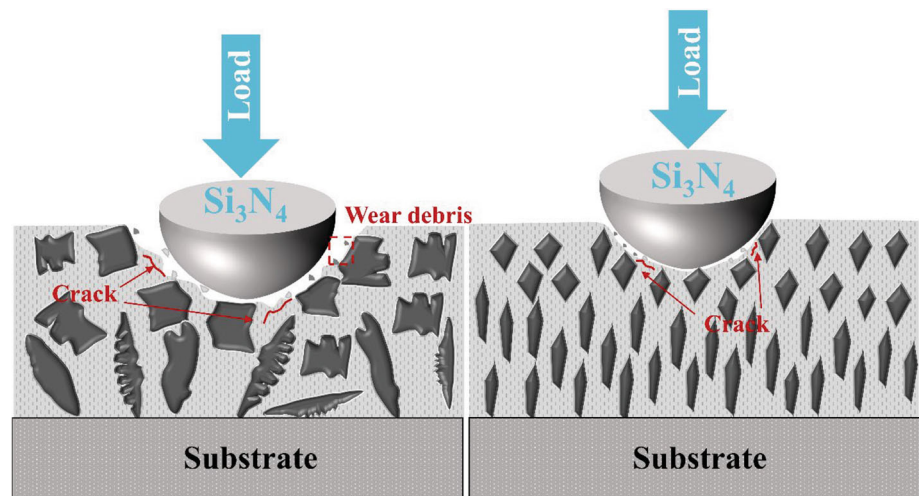
grain refinement of the internal structure and a larger grain boundary area in the fine microstructure. Thus, the strength and hardness were relatively high, and under the action of fine grain strengthening, the wear resistance of the coating improved.

Conclusions

In this study, CLA and EHLA were used to prepare an AlCoCrFeNi_{2.1} HEA coating. The influences of EHLA technology on the microstructures and properties of the coating and the corresponding strengthening mechanism were studied. The following conclusions were obtained:

- (1) The surface of the coating prepared by EHLA was flat, and the roughness was low (Ra (EHLA): 4.350 µm; Ra (CLA): 7.833 µm). The dilution rate decreased by 41% (EHLA: 39%, CLA: 66%); and the porosity decreased by 80% (EHLA: 0.2%, CLA: 1%).
- (2) A high cooling rate and solidification rate led to obvious microstructure refinement and a more uniform grain distribution in the EHLA coating. BCC phase precipitation was reduced by 22% (EHLA: 6.75%, CLA: 8.67%).
- (3) Under the action of fine-grain strengthening, the average microhardness and wear resistance of the EHLA coating improved to a certain extent. a) The hardness was increased by 15% (the EHLA coating reached 301 HV, and the CLA coating was 255 HV). b) The wear rate was reduced by 15% (the wear rates of the EHLA and CLA coatings were 6.19×10^2

Fig. 14 Wear mechanisms of the CLA and EHLA coatings: (a) CLA and (b) EHLA.



and $5.24 \times 10^2 \text{ mm}^3/(\text{N m})$, respectively). The wear mechanisms of the coating included adhesive wear, abrasive wear and oxidation wear.

Acknowledgments This research was financially supported by National Natural Science Foundation of China (Nos. 52005113, 52275366, 52203378), Tianjin Science and Technology Plan Project (22JCYBJC01590), and Young Talent Support Project of Guangzhou Association for Science and Technology (QT-2023-038).

Author Contributions JW contributed to investigation and writing-original draft. YL contributed to methodology and review & editing. BL and YC helped in investigation and data curation. JL and NT contributed to conceptualization, review & editing. YZ and ZL helped in investigation.

References

1. E.P. George, D. Raabe and R.O. Ritchie, High-Entropy Alloys, *Nat. Rev. Mater.*, 2019, **4**(8), p 515-534. <https://doi.org/10.1038/s41578-019-0121-4>
2. Y. Fu, J. Li, H. Luo et al., Recent Advances on Environmental Corrosion Behavior and Mechanism of High-Entropy Alloys, *J. Mater. Sci. Technol.*, 2021, **80**, p 217-233. <https://doi.org/10.1016/j.jmst.2020.11.044>
3. P. Sathiyamoorthi and H.S. Kim, High-Entropy Alloys with Heterogeneous Microstructure: Processing and Mechanical Properties, *Prog. Mater. Sci.*, 2022, **123**, 100709. <https://doi.org/10.1016/j.pmatsci.2020.100709>
4. X. Wang, W. Guo and Y. Fu, High-Entropy Alloys: Emerging Materials for Advanced Functional Applications, *J. Mater. Chem.*, 2021, **9**(2), p 663-701. <https://doi.org/10.1039/d0ta09601f>
5. J. Luo, W. Sun, R. Duan et al., Laser Surface Treatment-Introduced Gradient Nanostructured TiZrHfTaNb Refractory High-Entropy Alloy with Significantly Enhanced Wear Resistance, *J. Mater. Sci. Technol.*, 2022, **110**, p 43-56. <https://doi.org/10.1016/j.jmst.2021.09.029>
6. Y. Zhang, T.T. Zuo, Z. Tang et al., Microstructures and Properties of High-Entropy Alloys, *Prog. Mater. Sci.*, 2014, **61**, p 1-93. <https://doi.org/10.1016/j.pmatsci.2013.10.001>
7. Z. Lei, X. Liu, Y. Wu et al., Enhanced Strength and Ductility in a High-Entropy Alloy via Ordered Oxygen Complexes, *Nature*, 2018, **563**(7732), p 546-550. <https://doi.org/10.1038/s41586-018-0685-y>
8. S. Shajahan, A. Kumar, M. Chopkar et al., Oxidation Study of CoCrCuFeNiSix High Entropy Alloys, *Mater. Res. Express.*, 2020, **7**(1), 016532. <https://doi.org/10.1088/2053-1591/ab640a>
9. X.L. Shang, Z.J. Wang, F. He et al., The Intrinsic Mechanism of Corrosion Resistance for FCC High Entropy Alloys, *Sci. China Technol. Sc.*, 2018, **61**, p 189-196. <https://doi.org/10.1007/s11431-017-9114-1>
10. R.O. Ritchie et al., A Fracture-Resistant High-Entropy Alloy for Cryogenic Applications, *Science*, 2014, **345**(6201), p 1153-1158. <https://doi.org/10.1126/science.1254581>
11. J.Y. He, W.H. Liu, H. Wang et al., Effects of Al Addition on Structural Evolution and Tensile Properties of the FeCoNiCrMn High-Entropy Alloy System, *Acta Mater.*, 2014, **62**(1), p 105-113. <https://doi.org/10.1016/j.actamat.2013.09.037>
12. O.N. Senkov, G.B. Wilks, J.M. Scott et al., Mechanical Properties of Nb₂₅Mo₂₅Ta₂₅W₂₅ and V₂₀Nb₂₀Mo₂₀Ta₂₀W₂₀ Refractory High Entropy Alloys, *Intermetallics*, 2011, **19**, p 698-706. <https://doi.org/10.1016/j.intermet.2011.01.004>
13. Y. Lu, Y. Dong, S. Guo et al., A Promising New Class of High-Temperature Alloys: Eutectic High-Entropy Alloys, *Sci. Rep.*, 2014, **4**(1), p 6200. <https://doi.org/10.1038/srep06200>
14. I.S. Wani, T. Bhattacharjee, S. Sheikh et al., Ultrafine-Grained AlCoCrFeNi_{2,1} Eutectic High-Entropy Alloy, *Mater. Res. Lett.*, 2016, **4**(3), p 174-179. <https://doi.org/10.1080/21663831.2016.1160451>
15. Y. Lu, Y. Dong, H. Jiang et al., Promising Properties and Future Trend of Eutectic High Entropy Alloys, *Scripta Mater.*, 2020, **187**, p 202-209. <https://doi.org/10.1016/j.scriptamat.2020.06.022>
16. X. Gao, Y. Lu, B. Zhang et al., Microstructural Origins of High Strength and High Ductility in an AlCoCrFeNi_{2,1} Eutectic High-Entropy Alloy, *Acta Mater.*, 2017, **141**, p 59-66. <https://doi.org/10.1016/j.actamat.2017.07.041>
17. P. Shi, R. Li, Y. Li et al., Hierarchical Crack Buffering Triples Ductility in Eutectic Herringbone High-Entropy Alloys, *Science*, 2021, **373**(6557), p 912-918. <https://doi.org/10.1126/science.abf6986>
18. Y. Lu, X. Wu, Z. Fu et al., Ductile and Ultrahigh-Strength Eutectic High-Entropy Alloys by Large-Volume 3D Printing, *J. Mater. Sci. Technol.*, 2022, **126**, p 15-21. <https://doi.org/10.1016/j.jmst.2022.04.004>
19. Y. Zhang, J. Li, X. Wang et al., The Interaction and Migration of Deformation Twin in an Eutectic High-Entropy Alloy

- AlCoCrFeNi_{2.1}, *J. Mater. Sci. Technol.*, 2019, **35**(5), p 902–906. <https://doi.org/10.1016/j.jmst.2018.09.067>
20. W. Pan, P. Fu, Z. Li et al., Microstructure and Mechanical Properties of AlCoCrFeNi_{2.1} Eutectic High-Entropy Alloy Synthesized by Spark Plasma Sintering of Gas-Atomized Powder, *Intermetallics*, 2022, **144**, p 107523. <https://doi.org/10.1016/j.intermet.2022.107523>
 21. L. Zhu, P. Xue, Q. Lan et al., Recent Research and Development Status of Laser Cladding: A Review, *Opt. Laser Technol.*, 2021, **138**, 106915. <https://doi.org/10.1016/j.optlastec.2021.106915>
 22. Y. Liu, Y. Ding, L. Yang et al., Research and Progress of Laser Cladding on Engineering Alloys: A Review, *J. Manuf. Process.*, 2021, **66**, p 341–363. <https://doi.org/10.1016/j.jmapro.2021.03.061>
 23. Y. Guan, X. Cui, D. Chen et al., Realizing High Strength and Toughness of Gradient High-Entropy Alloy Coating by In-Situ Interface Reaction of FeCoCrNi/FeCoCrAl, *Surf. Coat. Technol.*, 2023, **464**, 129569. <https://doi.org/10.1016/j.surfcoat.2023.129569>
 24. A.A. Siddiqui and A.K. Dubey, Recent Trends in Laser Cladding and Surface Alloying, *Opt. Laser Technol.*, 2021, **134**, 106619. <https://doi.org/10.1016/j.optlastec.2020.106619>
 25. X. Wen, X. Cui, G. Jin et al., Corrosion and Tribo-Corrosion Behaviors of Nano-lamellar Ni_{1.5}CrCoFe_{0.5}Mo_{0.1}Nb_x Eutectic High-Entropy Alloy Coatings: The Role of Dual-Phase Microstructure, *Corros. Sci.*, 2022, **201**, p 110305. <https://doi.org/10.1016/j.corsci.2022.110305>
 26. X.L. Yan, S.Y. Dong, B.S. Xu et al., Progress and Challenges of Ultrasonic Testing for Stress in Remanufacturing Laser Cladding Coating, *Materials*, 2018, **11**(2), p 293. <https://doi.org/10.3390/ma11020293>
 27. O. Raykis, Alternative with a Future: High-Speed Laser Metal Deposition Replaces Hard Chrome Plating, *Laser Tech. J.*, 2017, **14**, p 28–30. <https://doi.org/10.1002/latj.201700006>
 28. T. Schopphoven, A. Gasser and G. Backes, EHLA: Extreme High-Speed Laser Material Deposition: Economical and Effective Protection Against Corrosion and Wear, *Laser Tech. J.*, 2017, **14**, p 26–29. <https://doi.org/10.1002/latj.201700020>
 29. Y. Liang, Z.Y. Liao, L.L. Zhang et al., A Review on Coatings Deposited by Extreme High-Speed Laser Cladding: Processes, Materials, and Properties, *Opt. Laser Technol.*, 2023, **164**, 109472. <https://doi.org/10.1016/j.optlastec.2023.109472>
 30. J. Zhou, Y. Cheng, Y. Wan et al., Solidification Characteristics and Microstructure of TaNbZrTi Refractory High Entropy Coating by Extreme High-Speed Laser Cladding, *Int. J. Refract. Met. H.*, 2023, **115**, 106257. <https://doi.org/10.1016/j.ijrmhm.2023.106257>
 31. Q. Yan, K. Yang, Z.D. Wang et al., Surface Roughness Optimization and High-Temperature Wear Performance of H13 Coating Fabricated by Extreme High-Speed Laser Cladding, *Opt. Laser Technol.*, 2022, **149**, 107823. <https://doi.org/10.1016/j.optlastec.2021.107823>
 32. Q. Zhang, Q. Wang, B. Han et al., Comparative Studies on Microstructure and Properties of CoCrFeMnNi High Entropy Alloy Coatings Fabricated by High-Speed Laser Cladding and Normal Laser Cladding, *J. Alloy. Compd.*, 2023, **947**, 169517. <https://doi.org/10.1016/j.jallcom.2023.169517>
 33. W. Yuan, R. Li, Z. Chen et al., A Comparative Study on Microstructure and Properties of Traditional Laser Cladding and High-Speed Laser Cladding of Ni45 Alloy Coatings, *Surf. Coat. Technol.*, 2021, **405**, 126582. <https://doi.org/10.1016/j.surfcoat.2020.126582>
 34. Y. Ding, W. Bi, C. Zhong et al., A Comparative Study on Microstructure and Properties of Ultra-High-Speed Laser Cladding and Traditional Laser Cladding of Inconel625 Coatings, *Materials*, 2022, **15**(18), p 6400. <https://doi.org/10.3390/ma15186400>
 35. A. Meghwal, S. Pinches, A. Anupam et al., Structure-Property Correlation of a CoCrFeNi Medium-Entropy Alloy Manufactured Using Extreme High-Speed Laser Material Deposition (EHLA), *Intermetallics*, 2023, **152**, 107769. <https://doi.org/10.1016/j.intermet.2022.107769>
 36. C. Du, L. Hu, X. Ren et al., Cracking Mechanism of Brittle FeCoNiCrAl HEA Coating Using Extreme High-Speed Laser Cladding, *Surf. Coat. Technol.*, 2021, **424**, 127617. <https://doi.org/10.1016/j.surfcoat.2021.127617>
 37. M. Liu, H. Jiang, G. Chang et al., Effect of Laser Remelting on Corrosion and Wear Resistance of Fe82Cr16SiB Alloy Coatings Fabricated by Extreme High-Speed Laser Cladding, *Mater. Lett.*, 2022, **325**, 132823. <https://doi.org/10.1016/j.matlet.2022.132823>
 38. B. Shen, B. Du, M. Wang et al., Comparison on Microstructure and Properties of Stainless Steel Layer Formed by Extreme High-Speed and Conventional Laser Melting Deposition, *Front. Mater.*, 2019, **6**, p 248. <https://doi.org/10.3389/fmats.2019.00248>
 39. G. Ma, B. Xu, H. Wang, X. Wang, G. Li and S. Zhang, Research on the Microstructure and Space Tribology Properties of Electric-Brush Plated Ni/MoS₂-C Composite Coating, *Surf. Coat. Technol.*, 2013, **221**, p 142–149. <https://doi.org/10.1016/j.surfcoat.2013.01.039>
 40. L. Zhang, Y. Ji, Q. Ye et al., An AlCoCrFeNi_{2.1} High-Entropy Alloy Coating with Uniform Microstructure and High Hardness, *Mater. Lett.*, 2023. <https://doi.org/10.1016/j.matlet.2023.134636>

Publisher's Note Springer Nature remains neutral with regard to jurisdictional claims in published maps and institutional affiliations.

Springer Nature or its licensor (e.g. a society or other partner) holds exclusive rights to this article under a publishing agreement with the author(s) or other rightsholder(s); author self-archiving of the accepted manuscript version of this article is solely governed by the terms of such publishing agreement and applicable law.